Journal of Geophysical Research: Earth Surface

RESEARCH ARTICLE
10.1029/2018JF004678

The Intermittency Regions of Powder Snow Avalanches

B. Sovilla[1], J. N. McElwaine[2], and A. Köhler[1]

[1]WSL Institute for Snow and Avalanche Research SLF, Davos Dorf, Switzerland, [2]Department of Earth Sciences, Durham University, Science Labs, Durham, UK

Key Points:
- Powder snow avalanche internal velocity shows mesoscale spatial and temporal coherence
- Coherent structure velocities may greatly exceed the velocity of the avalanche front
- Coherent structures have densities fluctuating between that of a dilute mixture of air and fine particles and that of a dense avalanche flow

Correspondence to:
B. Sovilla,
sovilla@slf.ch

Citation:
Sovilla, B., McElwaine, J. N., & Köhler, A. (2018). The intermittency regions of powder snow avalanches. *Journal of Geophysical Research: Earth Surface*, *123*, 2525–2545. https://doi.org/10.1029/2018JF004678

Received 16 MAR 2018
Accepted 23 SEP 2018
Accepted article online 27 SEP 2018
Published online 22 OCT 2018

Abstract Powder snow avalanches are typically composed of several regions characterized by different flow regimes. These include a turbulent suspension cloud of fine particles, a dense basal flow, and an intermittency frontal region, which is characterized by large fluctuations in impact pressure, air pressure, velocity, and density, but whose origin remains unknown. In order to describe the physical processes governing the intermittency region, we present data from four large powder snow avalanches measured at the Vallée de la Sionne test site in Switzerland, which show that the intermittency is caused by mesoscale coherent structures. These structures have a length of 3–14 m and a height of 10 m or more. The structures can have velocities as much as 60% larger than the avalanche front speed and are characterized by an air/particle mixture whose average density can be as high as 20 kg/m^3. This average density increases the drag on large granules by a factor of up to 20 compared to pure air, so that each structure can maintain denser snow clusters and single snow granules in suspension for several seconds. The intermittency region has importance for the dynamics of an avalanche, as it provides an efficient mechanism for moving snow from the dense layer to the powder cloud, but also for risk assessment, as it can cause large forces at large heights above the basal dense layer.

1. Introduction

A powder snow avalanche (PSA), or mixed avalanche (Issler et al., 1996), is a type of avalanche that includes a region where some snow grains are suspended by turbulence, forming a powder cloud which covers dense flow regimes moving underneath (Sovilla et al., 2015). They are closely related to turbidity currents (Meiburg et al., 2012) and pyroclastic flows, and they are a type of gravity current (Simpson, 1997).

In the past, PSAs were commonly thought to consist of a low-density, turbulent suspension layer above, and sometimes in front of, a dense flow (Norem, 1991; Zwinger et al., 2003). However, observations from the 1980s or earlier from Canada (Schaerer & Salway, 1980), Russia (Bozhinskiy & Losev, 1998; Grigoryan et al., 1982; Sukhanov, 1982), and Japan (Nishimura et al., 1993; Shimizu et al., 1980) have shown the existence of a third region, sometimes called the light flow layer or the saltation layer. In recent years there has been increasing evidence of this third region, which has characteristics of both a dense region and a suspension region. Issler et al. (1996) observed that in the deposit of three large powder avalanches it was possible to identify three deposit types that differed in granulometry, hardness, density, and stratification. In later work, Issler et al. (2008) demonstrated that these deposit types come from the dense, fluidized, and suspension regions.

In a review paper, Sovilla et al. (2015) used avalanche pressure, velocity, and density data to show that the generic structure of a PSA is considerably more complicated than a simple two layer model. PSAs feature distinct flow regions with a complex density stratification (Figure 1 upper panel); while the binary stratification between dense and suspension flow regimes may be realistic hundreds of meters behind the front, this clear distinction does not exist in the avalanche head.

Recently, new technologies have added information to the understanding of what happens inside fully developed power snow avalanches. Measurements performed with *GEODAR* (Ash et al., 2014), an innovative radar installed at the full-scale avalanche test site Vallée de la Sionne (VdlS), have shown that large powder avalanches exhibit multiple flow regimes simultaneously. One reason for this is that large avalanches tend to cover a great range of altitudes and therefore involve a wide range of snow conditions (Faug et al., 2018; Köhler et al., 2018).

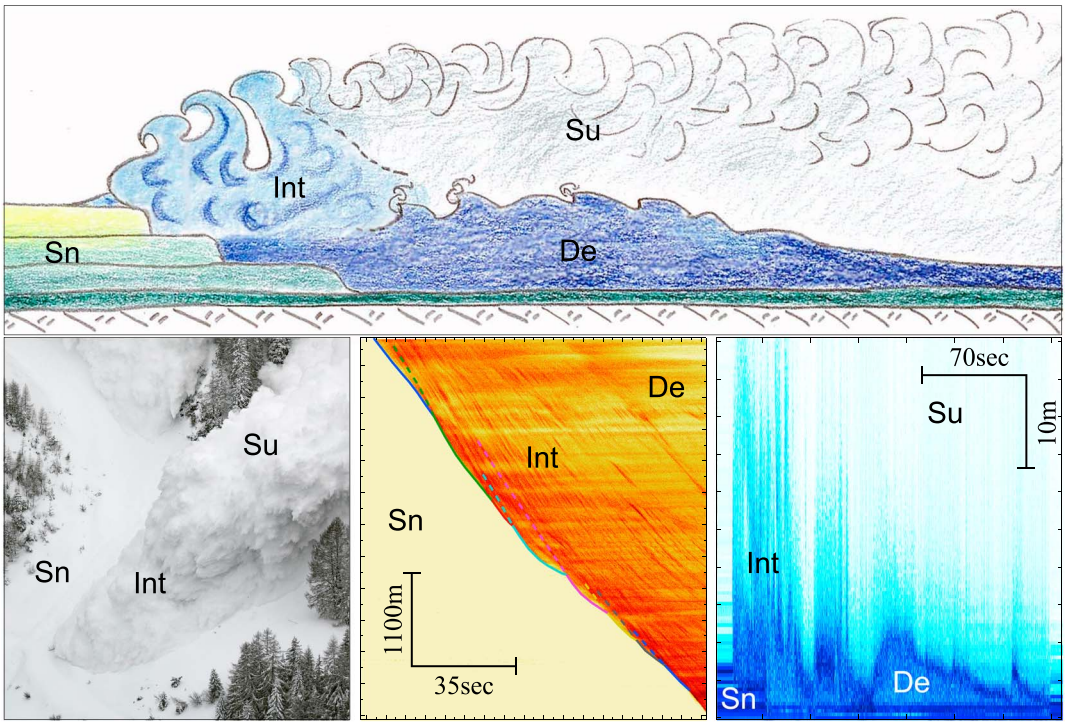

Figure 1. Upper panel: Schematic of a mixed powder snow avalanche entraining a generic layered snow cover (reproduced from Sovilla et al., 2015). Lettered regions correspond to: Int = the intermittency region; De = the basal dense layer; Su = the suspension layer; Sn = the static snow cover. The lower left panel shows a detail of the frontal dynamics of a large powder snow avalanche released at Vallée de la Sionne in 2017 (Photo: Yann Gross). The lower middle panel shows a detail of the avalanche frontal region measured with GEODAR in 2015 (Köhler et al., 2016). Both pictures show a complex surging activity in the avalanche frontal zone. The lower right panel shows an upward pointing frequency-modulated continuous-wave radar signal as a function of time for avalanche #20150016. In the lower panels, insets show the time-distance full extension of the axes.

In particular, researchers at VdlS observed that in the frontal region of a fully developed PSA, but sometimes also in the avalanche body, the radar data signature is characterized by short streaks lasting a few seconds (Figure 1 lower middle panel). These streaks were interpreted as an intense surging activity flowing faster than the avalanche front. Once the internal surges reach the front, they quickly decelerate and starve, giving the front an intermittent character (Köhler et al., 2016). As a consequence, researchers named this behavior the *intermittent flow regime*.

The concept of intermittency in PSAs is not new. Sharp fluctuations in avalanche dynamics variables have been observed frequently in the past. Frequency-modulated continuous-wave (FMCW) radars, installed along the avalanche path at the VdlS test site, have repeatedly demonstrated the presence of surges and highlight a frontal region characterized by large signal intensity well above the basal dense layer (Figure 1 bottom right panel).

Signal fluctuations are clearly visible in many earlier data sets. Measurements of impact pressure and air pressure performed in the 1980s in Japan indicated the presence of oscillatory behavior in the dilute avalanche regions (Shimizu et al., 1980). The presence of snow balls of different sizes at different heights in the avalanche frontal region was studied by Schaer and Issler (2001).

Nevertheless, a good understanding of the physical processes governing the intermittency flow regime and thus the dynamics of the avalanche frontal region is still missing (Issler et al., 2018). This is particularly important because the frontal region has the highest velocities and the largest pressures and is therefore typically the most destructive part of the flow (Köhler et al., 2016; Schaer & Issler, 2001; Sovilla, Schaer, Kern, et al., 2008).

Low-density gravity currents are usually modeled as Newtonian fluids (Konopliv et al., 2016) because the particle volume fraction is low. The snow grains are modeled by evolving a density field where it is assumed that the grains closely follow the air flow because the Stokes number is low. These models agree well with results

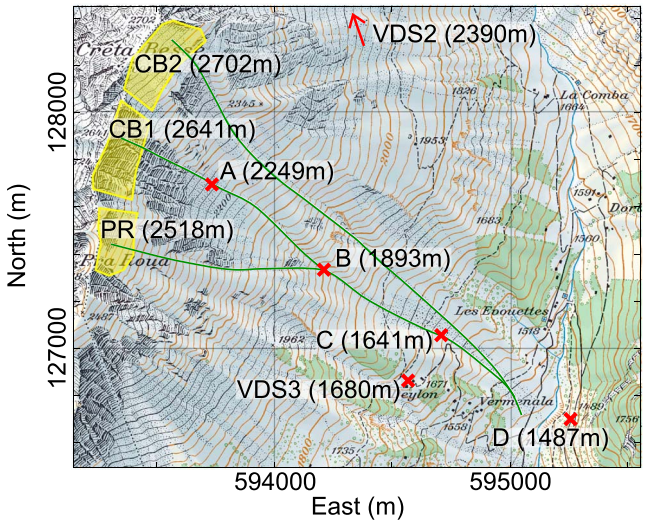

Figure 2. Overview of the Vallée de la Sionne test site. Yellow areas mark the location of the most probable release areas: PR, CB1, and CB2. The green lines show the corresponding avalanche trajectories. Red crosses mark the locations of the pylon (C), the caverns hosting the frequency-modulated continuous-wave radars (A, B, C), and the bunker hosting the GEODAR system (D). The base map was obtained from Swiss Geoportal [2015] with the Swiss coordinate system CH1903 (SRID 21781). CB1 = Crêta Besse 1; CB2 = Crêta Besse 2; PR = Pra Roua.

of laboratory experiments (Bonnecaze et al., 1996) and can accurately predict deposition patterns if a sedimentation velocity is included (Ancey, 2004). However, they do not describe the intermittent nature of the avalanche front.

Only recently, Issler and Gauer (2008) and later Bartelt et al. (2016) attempted to include the intermediate (average) density of the frontal region in their models. Intermittency was even built into the model proposed by Bartelt et al. (2016). Nevertheless, the physical description of the processes governing the fluctuations is today controversial (Issler et al., 2018).

In this paper we analyze avalanche pressure, air pressure, velocity, and density data of full-scale avalanches, focusing on the head region, in order to characterize and understand the origins of the intermittency in PSAs. We use the word intermittency in a very generic way to represent sharp fluctuations in dynamic variables such as pressure, density, velocity, and flow depth (Sanford, 1997). The data were collected at the VdlS avalanche test site, both with intrusive methods using instruments which are installed on a 20-m tall pylon and with radar devices installed in a bunker opposite the avalanche path and below the avalanche surface.

In section 2 we describe the measurement systems. In section 3 we present the data from four avalanches. We discuss the data in detail and provide our interpretation in section 4. Finally, we give our conclusions in section 5.

2. Experimental Site and Equipment

The full-scale avalanche experimental VdlS test site is located in the western part of Switzerland, close to the town of Sion (Ammann, 1999; Issler, 1999). Avalanches start from three main release areas, indicated in Figure 2 with the abbreviations PR (Pra Roua), CB1 (Crêta Besse 1), and CB2 (Crêta Besse 2), and follow a partially channeled track. The runout zone starts immediately below the channeled area, where a debris cone extends to the valley bottom. Large avalanches may partially climb the slope on the opposite side of the valley, where a concrete bunker accommodates radars and the data acquisition system (Figure 2 D).

Measurements of the internal flow parameters are performed on an oval-shaped steel pylon that is 20 m tall, 0.59 m wide, and 1.58 m long (Figures 2 C and 3). At the pylon, optical sensors make it possible to reconstruct flow velocities up to 6 m above the ground (Kern et al., 2009; Sovilla, Schaer, Kern, et al., 2008). Capacitance measurements are used to reconstruct the density distribution (Louge et al., 1997) from 0.9 to 3.9 m above the ground, and pressure cells are used to measure avalanche pressure up to 5.5 m above the ground. The

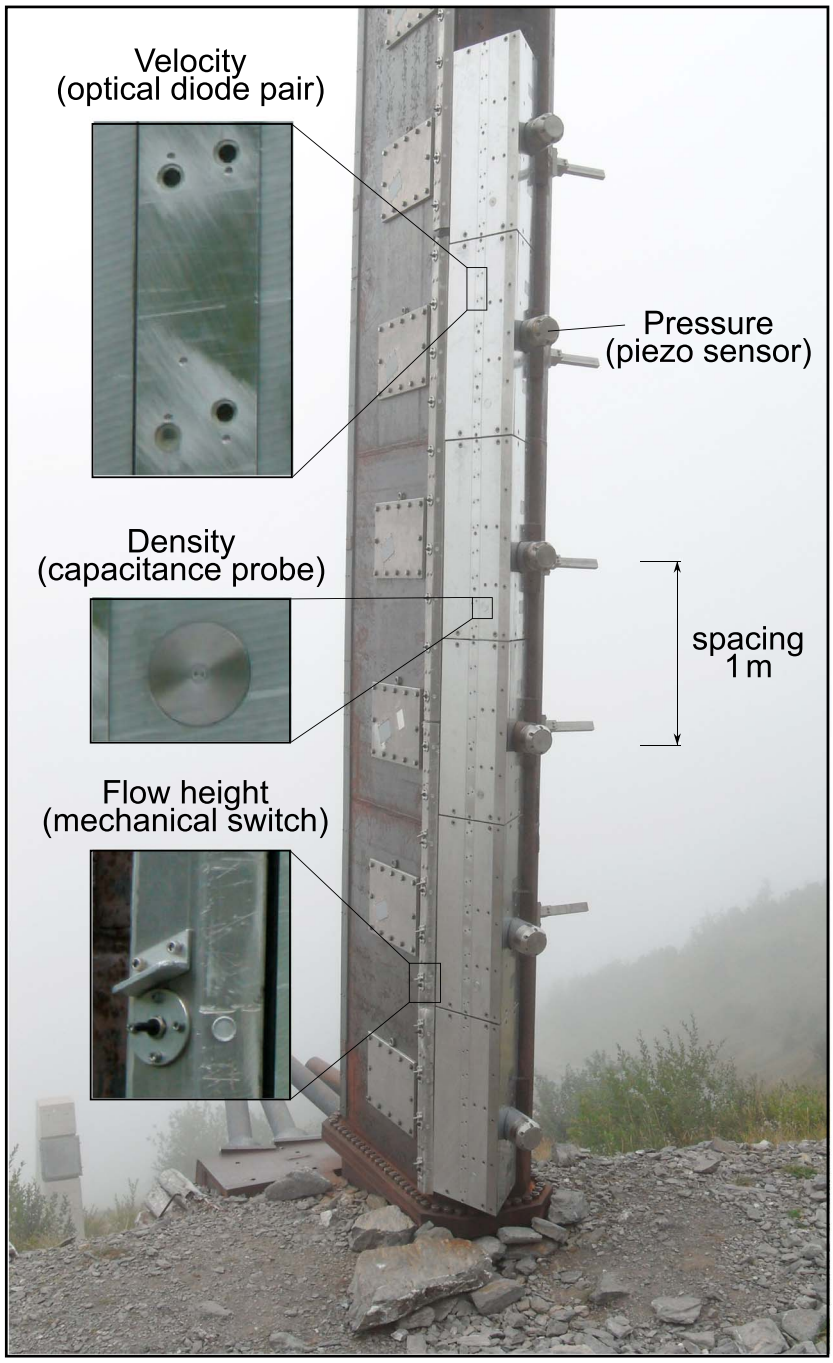

Figure 3. Overview of the 20-m-tall instrumented pylon at Vallée de la Sionne with the piezoelectric load cells. Close-up views are shown of optical sensors, capacitance probes, and flow height sensors. The air pressure sensor is out of view at 16 m.

flow height is measured with mechanical switches positioned at intervals of 0.1 m on the side of the pylon. A Pitot sensor installed 16 m above the ground measures the air pressure.

In addition to the intrusive technologies described above, caverns along the path host FMCW radars which are used to observe the avalanche structure and the erosion processes (Figure 2 A, B, and C). The bunker hosts the GEODAR, which provides information on the velocities along the path of the avalanche front and on internal structures like surging activity (Köhler et al., 2016; Vriend et al., 2013). Further, helicopter-based laserscanning

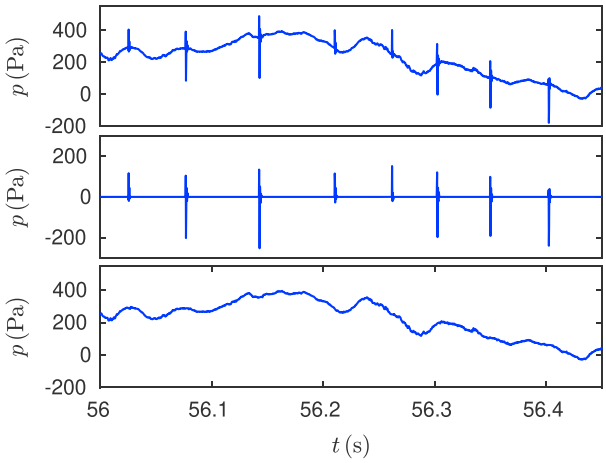

Figure 4. Avalanche #3017. (upper panel) Section of the air pressure signal including collisions. (Middle) Fitted impact signal. (Lower) Air pressure signal after removing impacts.

is used to map snow cover depths before and after an avalanche in order to calculate the avalanche mass balance (Sovilla et al., 2006, 2010).

2.1. Velocity Measurements

Velocity profiles, velocity fluctuations, and shear rates are inferred by cross-correlating optical backscattering signals between two closely spaced diodes (Dent et al., 1998; Kern et al., 2009). On the VdIS pylon, sensors with a 20 kHz sample frequency are located from the base of the mast up to a height of 6 m, with a vertical spacing of 125 mm. One of the avalanche data sets used in this paper (#816) refers to an older configuration with sensors installed at 2, 3, 4, and 5 m above ground. Sensors are placed flush with the sidewalls of wedges on the hillside face of the pylon (Figure 3). The wedge should ensure proper contact of the flow with the sensors and is designed to minimize flow disturbance and flow compression due to the flow around the blunt mast. This technology has proven to be successful in determining the velocity of snow granules and particle clusters, but it is less efficient in measuring velocity in dilute snow clouds where the homogeneous powder suspension does not have enough structure to be detected by the optical sensors (Kern et al., 2009). The greatest limitation of the sensor installation at VdIS is that it cannot resolve the vertical and transverse velocity of the particles.

2.2. Pressure Measurements

Avalanche pressure is measured with six piezoelectric load cells, hereafter designated as piezo sensors. They are installed on the uphill face of the pylon from 0.5 to 5.5 m above the ground, with 1 m vertical spacing (Figure 3). The sampling frequency is 7.5 kHz and the sensors have a diameter of 0.10 m and an area of 0.008 m^2. The measurement range of the pressure is 0–25 MPa.

Ten meters away from the pylon, another four high-frequency (5 to 7.5 kHz) pressure sensors are installed on a hollow steel beam with a rectangular cross-section (impact surface: 0.24 × 4.5 m) at 1.3, 2.3, 3.3, and 4.3 m above the ground (Sovilla, Schaer, & Rammer, 2008).

2.3. Air Pressure Measurements

Air pressure measurements were taken with one sensor mounted 16 m above the ground. The system is the same as described in McElwaine and Turnbull (2005) except that the transducer has been changed to a Validyne DP105 with a range of ±5 kPa and the sampling occurs at 5 kHz. This transducer has a high-frequency response and is resistant to water and ice. The transducer is connected by several short tubes to the surface of the sensor so that it measures the approximate static pressure in the flow. However, there is still some dependence on the speed and direction of the incoming flow. The transducer is mounted rigidly within a stiff assembly (a steel cylinder and plastic hemisphere) and is sensitive to impacts. An impulsive impact on the sensor assembly gives rise to a rapidly decaying oscillation lasting a few milliseconds that is well fitted by a simple harmonic oscillator with fixed frequency and damping, but unknown impact time and strength. Each collision is fitted, using least mean squares, and then the impacts can be removed from the data. This is shown in Figure 4 where the upper panel shows the air pressure signal including collisions, the middle panel shows the fitted collisions, and the lower panel shows the air pressure signal after subtracting the fitted collisions. The next step is to decompose the signal into different frequency bands using a Gaussian filter bank. This often reveals a dominant low frequency indicating a mesoscale coherent (MSC) structure (e.g., Figure 5). We extract this part of the signal using a parametric technique as follows. For simplicity we treat time as a continuous variable. The fitting procedure is based around finding the n times, $\{t_k\}$, of the maxima and minima and the amplitudes $\{A_k\}$ at these points. The phase at these consecutive turning points is

$$\phi_k = \phi(t_k) = k\pi. \tag{1}$$

We then define a continuous phase function $\phi(t)$ through these points using a cubic interpolation. Similarly, we define a continuous function $A(t)$ for the (positive) amplitudes at these points $\{A_k\}$ such that

$$A(t_k) = A_k. \tag{2}$$

The $2n$ parameters $\{t_1 \dots t_n\}$ and $\{A_1 \dots A_n\}$ are then optimized by minimizing

$$L = \int_0^T [p(t) - A(t)\sin\phi(t)]^2 \, dt. \tag{3}$$

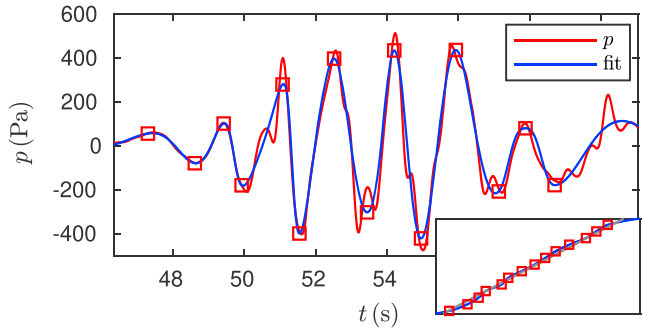

Figure 5. Avalanche #3017. Comparison of low frequency air pressure signal with the fitted function $A \sin \phi$. The fit points (t_k) are shown by red squares. The almost linear phase function $\phi(t)$ is shown in the inset panel demonstrating an almost constant frequency.

The results for #3017 are shown in Figure 5. The fit is also shown with the unfiltered data in Figure 16.

2.4. Density Measurements

Instantaneous snow densities are recorded with capacitance instruments attached to the pylon at 0.9, 1.9, 2.9, and 3.9 m above the ground, close to the optical sensors (Figure 3). With proper calibration for the VdIS basin (Louge et al., 1997), these probes detect how much material resides in their measurement volume (10 mm^3). Because snow is not distributed homogeneously and because the response of these probes is not linear with density, signal interpretation is not straightforward. However, by exploiting their relatively fast 7.5 kHz sampling frequency, one may inspect signal fluctuations and discern whether they are produced by a homogeneous suspension, a particle cluster, or an aggregate.

While this technique produces accurate records of the dielectric permittivity, its principal challenge is to relate local measurements of the dielectric constant to snow density. Snow characteristics, and thus the dielectric properties of snow, changes from the head to the tail of an avalanche. In our calculation, we use an averaged calibration curve that is valid for dry snow characterized by partly decomposed precipitation particles that we expect to be present in large quantities in PSAs. This simplification may introduce an error in the density calculation, which we estimate to be up to 20%.

A further well-known difficulty with density measurements is the instability produced by the amplifier, which is specific to the dielectric behavior of snow (Louge et al., 1997). The instabilities may disrupt provision of the sensor surface with stable currents of constant amplitude and manifest themselves as sudden jumps in the output voltage to incoherent values that cannot correspond to natural snow density signals and are easy to detect and remove. Nevertheless, as a result of the instabilities, it is very rare to record complete data sets of density.

2.5. GEODAR

GEODAR is a FMWC phased-array radar system that is installed in the bunker at VdIS (Ash et al., 2014). The radar has a center frequency of 5.3 GHz and a bandwidth of 200 MHz, that is, the frequency spans 5.2 – 5.4 GHz. Since the average wavelength (57 mm) is much larger than individual snow grains, it penetrates, with little attenuation, the suspension cloud, which is composed of crystals a few millimeters in diameter (Rastello et al., 2011). The radar records the movement of any snow balls or blocks larger than the order of a wavelength, thus giving important information on dense flow features that are present in the intermittency region.

The radar averages overall points at the same line-of-sight distance from the antenna. The range resolution is 0.75 m, and a complete view of the slope is collected at 111 Hz. A detailed description of the measurement principle and the radar design considerations can be found in Ash et al. (2014). Here we present data collected with the GEODAR Mark III system (Köhler et al., 2016).

Moving Target Indication (MTI) plots are used to display data collected with the GEODAR. These MTI plots are space-time plots that show the change in radar reflectivity at a particular time and range. The MTI plots differentiate between moving and nonmoving parts of the flow. Where there is no moving snow the plot is yellow or lightly colored. The transitions to a darker color intensity represent the arrival of avalanche fronts, and the change in value with time of these edges represent the approach velocities toward the radar (Köhler et al., 2016).

Lines of maximum darkness in MTI plots correspond to surges or waves in the avalanche. Because the plots show the average across the slope, lines and edges can cross each other when they correspond to features at different lateral locations (Vriend et al., 2013). In this paper the MTI plots are used as an interpretation tool for the measurements collected at the pylon and to calculate the velocity of the avalanche front.

2.6. FMCW

Three FMCW radars are installed along the path in caverns A, B, and C (Figure 2). These radars point upward; they can create images of layers in the snow cover and observe the flowing snow as it passes over them. They give a qualitative picture of entrainment, deposition, and flow height (Gubler & Hiller, 1984; Sovilla et al., 2006). They additionally provide an excellent picture of the avalanche structure and are used in this paper to

Table 1
Avalanche and Snow Cover Data

Avalanche	#816	#20150016	#20163017	#20150003
Date (dd.mm.yy)	06.03.06	03.02.15	18.01.16	27.12.14
Time (hh:mm)	10:00	10:20	10:41	20:18
Size	Large	Large	Large	Large
Release type	Artificial	Artificial	Artificial	Spontaneous
Release zone	PR	PR	CB2	CB1
Intermittency region length at the pylon (m)	500	90	>120	15
MSCs characteristic size (m)	—	2–5	3–14	2–4
Snow depth at VDS2, H_t (m)	3.0	2.1	2.3	1.2
Snow depth at VDS3, H_b (m)	1.4[b]	0.9	1.0	0.75
Snow depth increase at VDS2, Δ_t (m)	1.2	1.0	1.2	0.7
Snow depth increase at VDS3, Δ_b (m)	0.6[b]	0.5	0.9	0.6
Average snow temperature, T_{50t} (° C)[a]	−6.2	−9.7	−11.5	−9.2
Average snow temperature, T_{50b} (° C)[a]	−2.0[b]	−3.5	−4.0	−6.4

Note. Snow cover information corresponds to the measurements performed at the weather stations VDS2 and VDS3 located at the top ($_t$) and bottom ($_b$) of the avalanche, respectively. For avalanche #816 the lower station data correspond to measurements at the nearest weather station Montana (MVE, 1,427 m above sea level). MSCs is the abbreviation for mesoscale coherent structures. The snow depth increase is measured over a time interval that varies among avalanches and corresponds to the duration of the new snow precipitation previous to the release. PR = Pra Roua; CB1 = Crêta Besse 1; CB2 = Crêta Besse 2. [a]Modeled, [b]Montana weather station.

visualize the intermittency region. The FMCW radars have a vertical resolution of around 100 mm and sample at 40 Hz. Their range is set to about 10 m.

2.7. Snow Cover Measurements and Modeling

Information on snow cover near VdlS is obtained from two weather stations. The weather station VDS2 at 2,390 m above sea level (asl) is used as a proxy for the conditions in the release area, and the weather station VDS3, close to the pylon at 1,680 m asl, is used to reconstruct the snow cover in the deposition area (Figure 2). The weather station VDS3 has not yet been installed at the time of avalanche #816, and proxy data were obtained from the closest representative station, Montana (MVE, Meteo Swiss), which is situated at an altitude of 1,427 m asl, 7 km in linear distance from VDS3. We used the numerical model SNOWPACK to reconstruct the snow properties for each avalanche event (Lehning et al., 2002). As a first approximation, we define the uppermost 0.5 m of the snow cover as representative of the snow properties of the avalanche. Snow properties are averaged over this depth, and the simulated snow temperature at the top (T_{50t}) and bottom (T_{50b}) stations are summarized in Table 1.

Note that the snow cover reconstructed at the weather stations can differ from the actual conditions in the flow path because earlier avalanche activity and entrainment/deposition can alter the old snow cover significantly (Steinkogler et al., 2014).

3. Results

In this section we describe data from the frontal region of four fully developed PSAs at VdlS. Following the classification of Köhler et al. (2018), the investigated avalanches were characterized by three coexistent flow regimes, namely intermittent, cold dense, and suspension. All four avalanches are large (Canadian avalanche-size classification; Jamieson, 2000). We refer to the avalanches by their archive number to allow comparison with other publications. We chose these four avalanches to illustrate the range of behavior and the variability that can occur. Here we briefly describe the four avalanches before going into more detail about each one.

- Avalanche #816: The largest avalanche we discuss, with a fully developed intermittency region that extends for several hundred meters. This avalanche was chosen as the largest that has occurred at VdlS with good data.

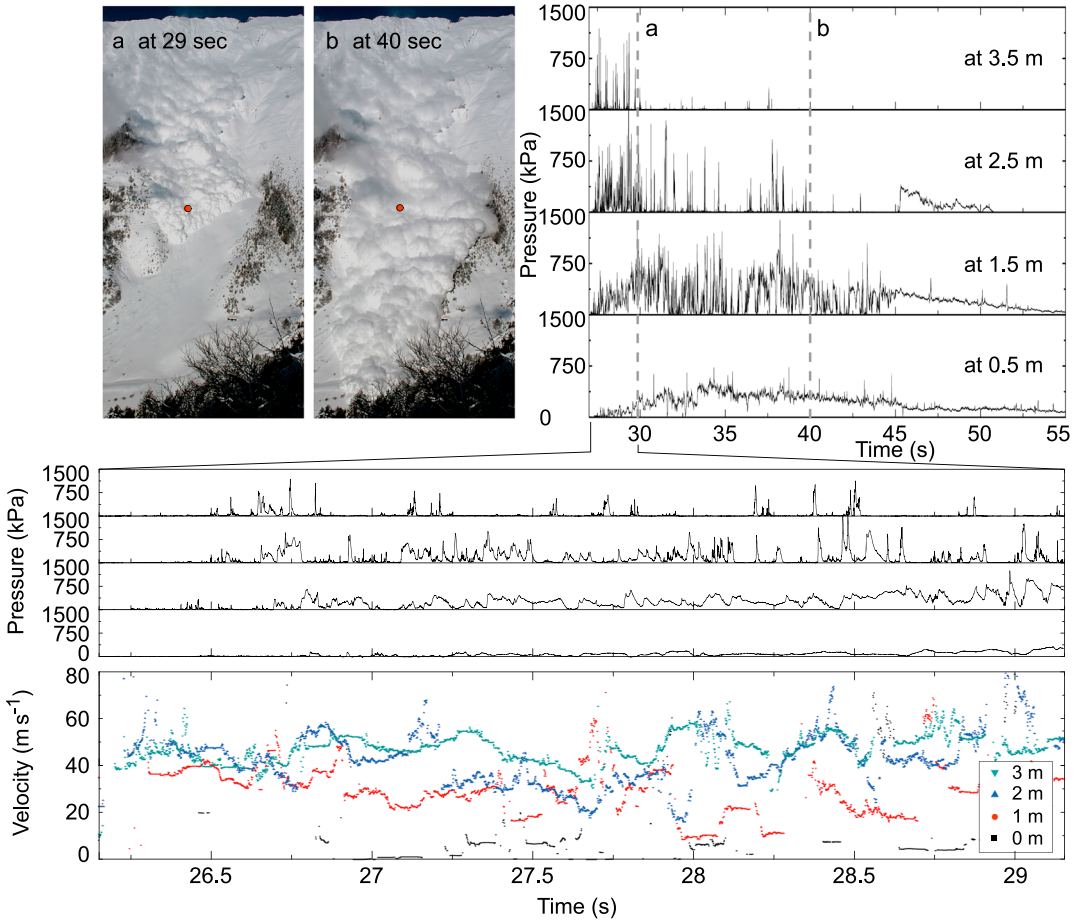

Figure 6. Avalanche #816. Photograph (a) was taken after the tallest part of the intermittency region passed the pylon. Photograph (b) was recorded when the last part of the intermittency region passed the pylon. The upper right panel shows pressure values at the pylon, where the vertical dotted lines correspond to the photographs (a) and (b). Pressures measured from 0.5 to 3.5 m above the sliding surface are displayed one over the other for a better estimation of the vertical distribution of the intermittency region. As a first approximation, we assume the sliding surface is positioned 0.50 m below the lower pressure sensor impacted by the flow. The middle panel shows zoomed-in view of the pressure measurements at the avalanche front. The lower panel shows the corresponding velocities.

- Avalanche #20150016: A large avalanche with a relatively short intermittency region that is closely coupled to the dense basal layer. This avalanche was chosen to illustrate this coupling and because a complete data set is available.
- Avalanche #20163017: A large avalanche with an intermittency region that is decoupled from the dense basal layer. This avalanche was chosen to show that the dynamics of the intermittency region can also be independent from the dense basal layer.
- Avalanche #20150003: A large avalanche where the intermittency region collapses and deposits in the region of the pylon. This avalanche was chosen to show what happens to the intermittency region in the deposition phase.

3.1. Avalanche #816

On 6 March 2006 two PSAs were artificially released. Avalanche #816 was the first and was released at 10:00 from PR. It descended past the pylon and climbed up the opposite slope to the bunker (Figure 6).

During the preceding 5 days there was 1.2 m of new snow in the release zone, bringing the total snow depth to 3.0 m. In the deposition zone the total snow depth was 1.4 m and the new snow precipitation was 0.6 m (Table 1). In the days preceding the experiment the air temperature oscillated between −20 and −2.8° C, preventing the consolidation of the new snow and resulting in an unstable snow cover. The average snow cover temperature of the uppermost 0.5 m, calculated with the model SNOWPACK, was −6.2° C in the release

zone and −2° C in the deposition zone, and thus the avalanche can be regarded as cold (Steinkogler et al., 2015). Note that for this avalanche snow cover information in the deposition zone was taken from the Montana weather station, which is located 7 km away at the same elevation.

Pressure measurements at the pylon indicate that this avalanche had a large intermittency region that lasted around 12 s, with local pressure peaks of over 1,000 kPa (Figure 6). During the first 3 s of signal, the intermittency reached at least 5.5 m above the ground (around 3.5 m above the avalanche sliding surface). It was probably even higher, but no pressure measurements were made higher than 5.5 m for this avalanche. The height of the intermittency region then decreased over time. Note that spikes of maximum pressure are not local but instead appear almost simultaneously, or with a very small time shift, over a large part of the avalanche flow depth (Figure 6 middle panel). In 2006, velocity measurements were performed at heights of 2, 3, 4, and 5 m above the ground. The measurements performed in the intermittency region are shown in detail in the bottom panel of Figure 6. The avalanche velocity fluctuated around 40 m/s. Velocities at the lowest sensor were typically lower than 10 m/s and the velocity generally increased with height, even though there were short time intervals with negative shear rates. Considering an average velocity of 40 m/s in the first 12 s of measurements, the extension of the intermittency region at the pylon was close to 500 m. There is no GEODAR data for this avalanche because the radar was first installed in 2010.

3.2. Avalanche #20150016

On 3 February 2015 four PSAs were artificially released at VdlS. Avalanche #20150016 was the first and was released at 10:20 from PR. The avalanche hit the pylon and descended another 600 m before stopping at the valley bottom. During the preceding 5 days there was 1.0 m of new snow in the release zone, bringing the total snow depth to 2.1 m. In the deposition zone the new snow amounted 0.5 m and the total snow depth was 0.9 m (Table 1). The average snow cover temperature of the uppermost 0.5 m calculated with the model SNOWPACK was −9.7° C in the release zone and −3.5° C in the deposition zone; the avalanches can thus be regarded as cold.

Secondary releases along the path resulted in several major surges, which were observed with the GEODAR radar (Figure 7). The avalanche at the pylon was characterized by distinct surges. The front missed the pylon. The first surge to hit the pylon was surge #1 in Figure 7, which dissipated around 50 m after the pylon. The second surge to hit the pylon was surge #2, which merged with the front at a range of 500 m.

At the pylon, this avalanche was characterized by two main intermittency regions. The first intermittency region was located immediately behind the front of surge #1 and lasted around 3 s (Figure 7 lower panel, #1, #2, and #3). This is also seen in the pressure measurements in Figure 7 (middle panel), which are characterized by the typical large fluctuations and spikes. A second intermittency episode was recorded by the pressure sensor 2.5 m above the sliding surface in the interval 99–104 s, while the lower two sensors show typical dense flow signals (Figure 7 lower panel, #5 and #6). This episode belonged to a major surge visible in the GEODAR data. Owing to low quality of the velocity measurements in the avalanche body, this second region is not analyzed further in this paper.

Figure 8 shows measurements of pressure and velocity corresponding to the first intermittency region of avalanche #20150016. The upper panel shows pressure at different heights above the sliding plane, displayed one over the other to facilitate interpretation of the signal. Avalanche pressure measurements are directly compared with the corresponding velocity measurements (lower panel). Velocity data show that surge #1 is considerably slower than surge #2. The velocity field appears to be discontinuous and is organized into coherent regions that correspond well to the spikes of maximum pressure. Considering an average velocity of 30 m/s in the first 3 s of measurements, the extent of the intermittency region at the pylon was about 90 m.

As with avalanche #816, spikes of maximum pressure are not local but appear, with a very small time shift, over a large part of the avalanche flow depth. Further, the pressure peaks appear to be synchronized in time with the coherency in the velocity signal, for example, at 92 s in Figure 8. This finding shows that this intermittency in pressure does not arise solely from the uncorrelated motion of individual large granules and that coherent structures are significant.

3.3. Avalanche #20163017

At 10:41 on 18 January 2016 a large PSA was artificially released from CB2. The avalanche flowed past the pylon and descended another 700 m, reaching the bunker.

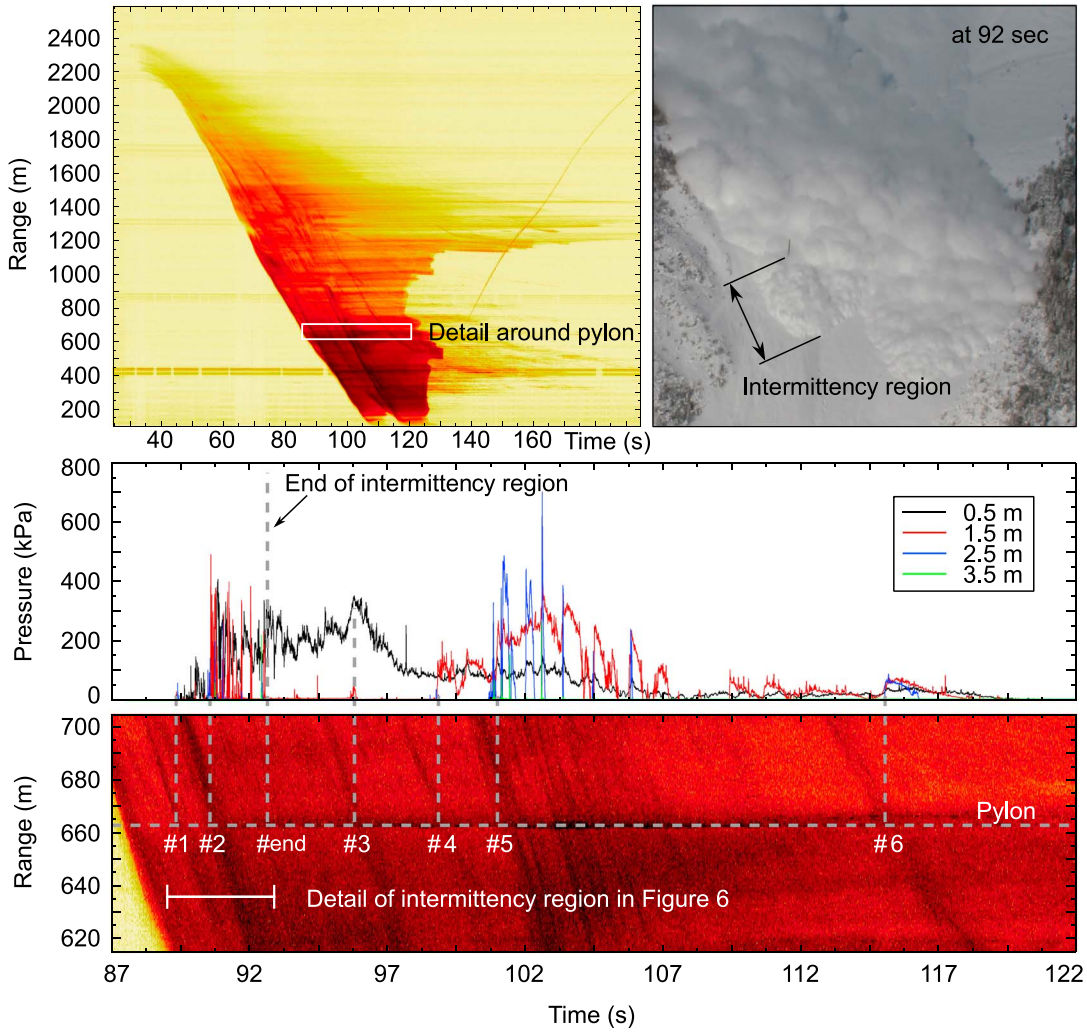

Figure 7. Avalanche #20150016. The upper panels show the GEODAR plot (left) and a photograph taken when the intermittency region had just passed the pylon (right). The arrow in the photograph indicates the approximate extension of the region with intermittency. The middle panel shows the avalanche pressure measured at different heights above the sliding surface. As a first approximation, we assume the sliding surface is positioned 0.50 m below the lower pressure sensor impacted by the flow. The lower panel shows a detail of the GEODAR data (corresponding to the white-framed rectangle in the upper left panel) at the pylon location with all surges that reached the obstacle zone identified (from #1 to #6). The photograph of the avalanche is synchronized in time with the pressure signals and the GEODAR details (vertical dashed lines).

The avalanche occurred 5 days after a large snowfall of 1.2 m in the release zone, which resulted in a total snow depth of up to 2.3 m (Table 1). In the deposition area the new snow was 0.9 m and the total snow depth was 1.0 m. The average snow cover temperature of the uppermost 0.5 m, calculated with the model SNOWPACK, was −11.5° C in the release zone and −4.0° C in the deposition zone, and thus the avalanche can be regarded as cold.

Even though the pylon was in the middle of the avalanche (Figure 9 middle panel), there was no deposit from the dense core, suggesting that only the dilute regions of the flow reached the pylon. Instead, traces of denser flow were left around the concrete wall and the wedge (Figure 9 right panel).

Figure 10 shows the pressure measured at the pylon (upper panel) and wedge (lower panel), as well as the corresponding 2-D velocity field measured at the pylon (middle panel). The measurements shown in Figure 10 suggest that an initial intermittency region lasted at least 4 s. As expected, the pressure measured at the wedge indicates impact with the denser region of the flow (lower panel, bottom line), while the pressure at the pylon only displays spikes typical of the intermittency region. The velocity data again show a discontinuous velocity field where MSC structures can be visually identified. Considering an average velocity of 30 m s in the first 4 s of measurements, the intermittency region at the pylon was at least 120 m long.

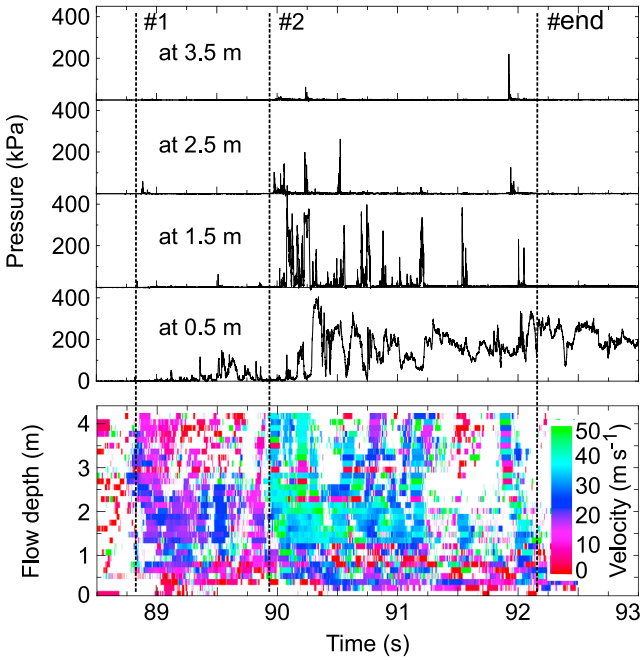

Figure 8. Avalanche #20150016. The upper panel shows the avalanche pressure measured in the intermittency region. The lower panel shows the corresponding velocity. #1 marks the front of the first surge hitting the pylon, #2 marks the front of the second surge hitting the pylon, and #end marks the end of the intermittency region at the pylon (corresponding to the lower panel in Figure 7).

A few seconds later another intermittency region arrived that reached the air pressure sensor at a height of 16 m on the mast (Figure 11). This registered on the air pressure transducer as a series of individual impacts that gave rise to a very high frequency ringing, which was only just resolved by the 5 kHz sampling frequency. The upper panel of Figure 11 shows the reconstructed series of impacts including a close-up view of an individual collision. These signals are completely different from the smooth and slowly varying signals due to air pressure variation and can be distinguished easily. The lower panel shows the amplitudes of these collisions averaged over time.

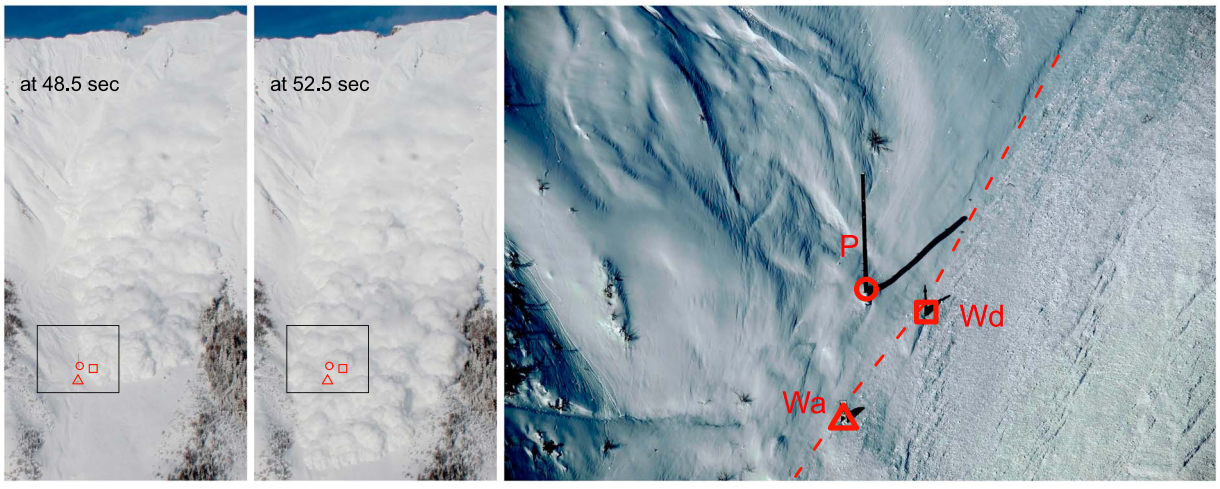

Figure 9. Avalanche #20163017. The left two photographs show the avalanche at first impact with the pylon and 4 s thereafter. The right photograph shows the avalanche deposit around the obstacles immediately after the avalanche passed. The red dashed line highlights the boundary of the denser flow with the typical sharply defined perimeter and granular structure. The P is outside the denser deposit while the Wd and the Wa were hit by the denser layer. P = pylon; Wd = wedge; Wa = wall.

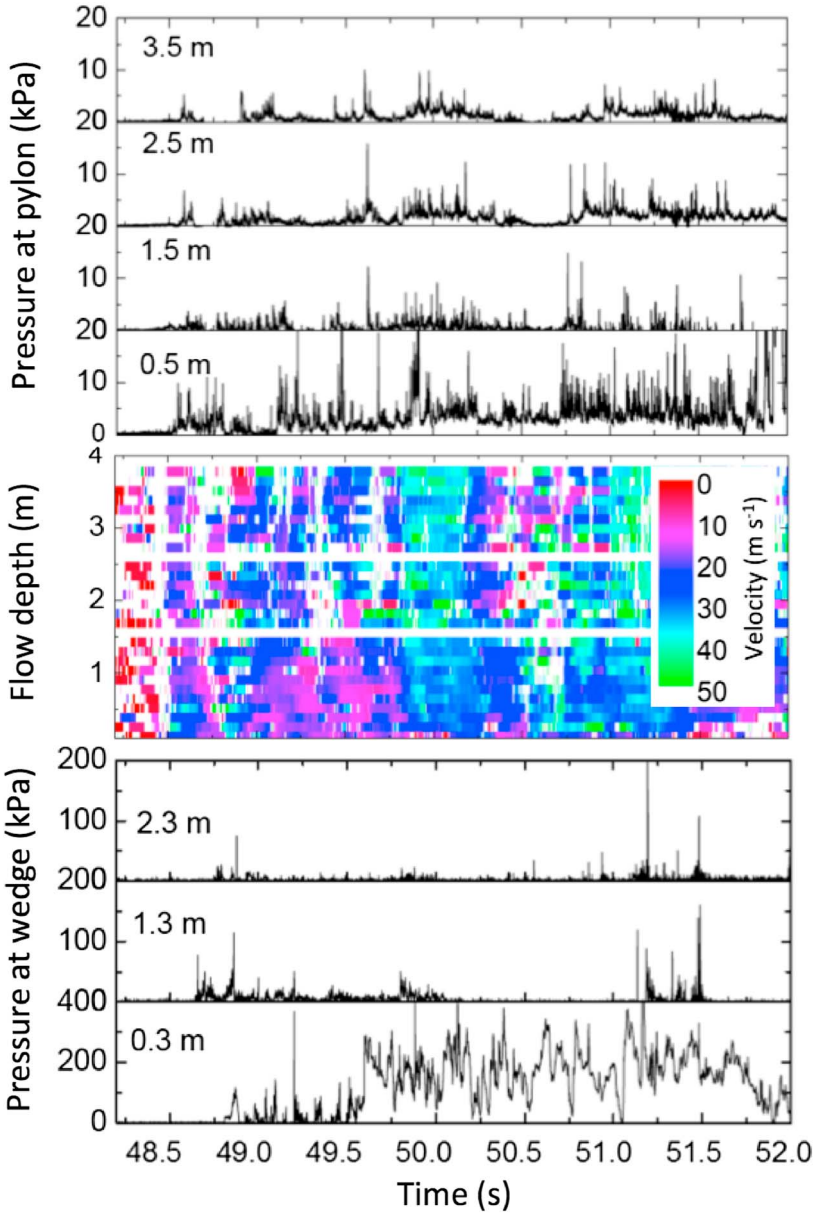

Figure 10. Avalanche #20163017. The upper and lower panels show the pressures measured at the pylon and at the wedge, respectively. The middle panel shows the corresponding avalanche velocity measured at the pylon.

3.4. Avalanche #20150003

Avalanche #20150003 naturally released at 20:18 on 27 December 2014. We cannot say with certainty where the avalanche originated, but the most probable location is CB1. A photograph taken on the morning of 29 December shows superficial traces of debris consistent with the occurrence of a large powder avalanche with a small dense core that stopped shortly below the pylon. The GEODAR plot in Figure 12 shows that the front moved past the pylon (a distance of 675 m from the bunker) and traveled another 50 m. The avalanche produced only a very weak air pressure signal that is not discussed further in this paper.

The avalanche released after an intense 24 hr of snow precipitation. In the release zone there was 0.7 m of new snow, which increased the total snow depth to 1.2 m. In the deposition zone there was 0.6 m of new snow and the total snow depth was 0.75 m. The average snow cover temperature of the uppermost 0.50 m, calculated with the model SNOWPACK, was −9.2° C in the release zone and −6.4° C in the deposition zone; the avalanche can thus be regarded as cold.

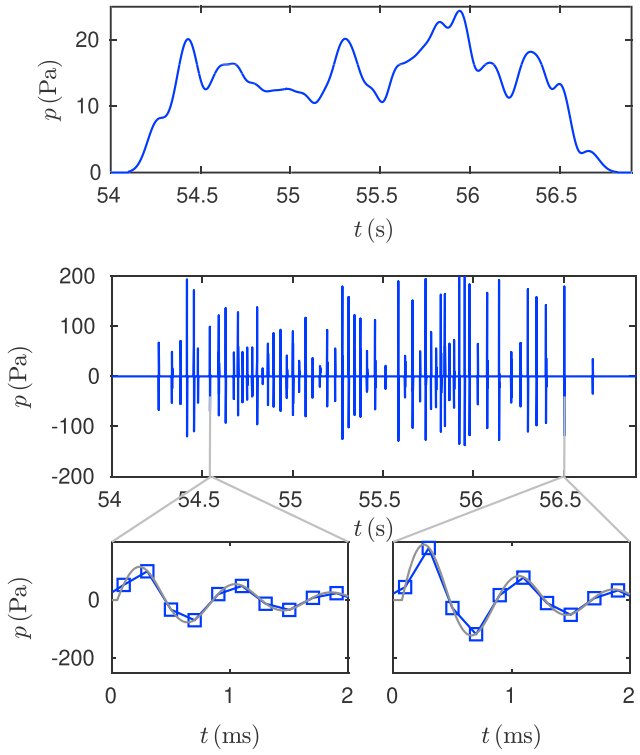

Figure 11. Avalanche #20163017. (upper panel) Individual granule impacts on the air pressure sensor at 16 m height. (middle panels) Two individual impacts showing the best fit simple harmonic oscillator functions. The squares correspond to the sampling points at a frequency of 5 kHz. (lower panel) The impacts averaged over time. The impacts are produced by high-density granules transported by a large structure a few seconds after the main front reached the obstacles.

The right panels of Figure 12 show the velocity, pressure, and density measured at the pylon. The intermittency region at the pylon lasted about 1 s, with spikes of pressure up to around 30 kPa. Considering an average velocity of 15 m/s during 1 s of measurements, the extent of the intermittency region at the pylon lasted only about 15 m before starving.

4. Discussion

The data presented in section 3 show that the avalanche frontal region is characterized by intermittency in pressure, density, and velocity. In particular, the velocity data show the presence of MSC structures whose number and duration vary significantly among avalanche events. The MSC structures are larger and more numerous when both new snow and snow cover depth are largest (Table 1). Note that the snow depths measured at the weather station may be different from the snow depth along the flow path, because previous avalanche activity may have considerably changed the underlying, older snow cover (Steinkogler et al., 2014).

4.1. Coherent Structures in the velocity Data

The upper panel of Figure 13 shows typical velocity profiles corresponding to mesoscale structures in the avalanche frontal region. In this specific example, the structures are detached from the denser basal layer and the velocity profiles correspond to the frontal structure (middle panel) and the fastest structure in avalanche #20163017 (lower panel). Error bars are used to indicate the velocity distribution inside each mesoscale structure and correspond to the 25–75% quantiles.

Mesoscale structures are normally characterized by a quasi-vertical velocity profile but particles in a structure have various speeds, as evidenced by the spread of the 25% and 75% percentiles of velocity at many measurement heights.

Internal structures are normally faster than frontal structures, and thus faster than the avalanche front (Köhler et al., 2016). For example, the largest internal structure at the pylon for avalanche #20163017 is 60% faster than the corresponding frontal structure (Figure 13).

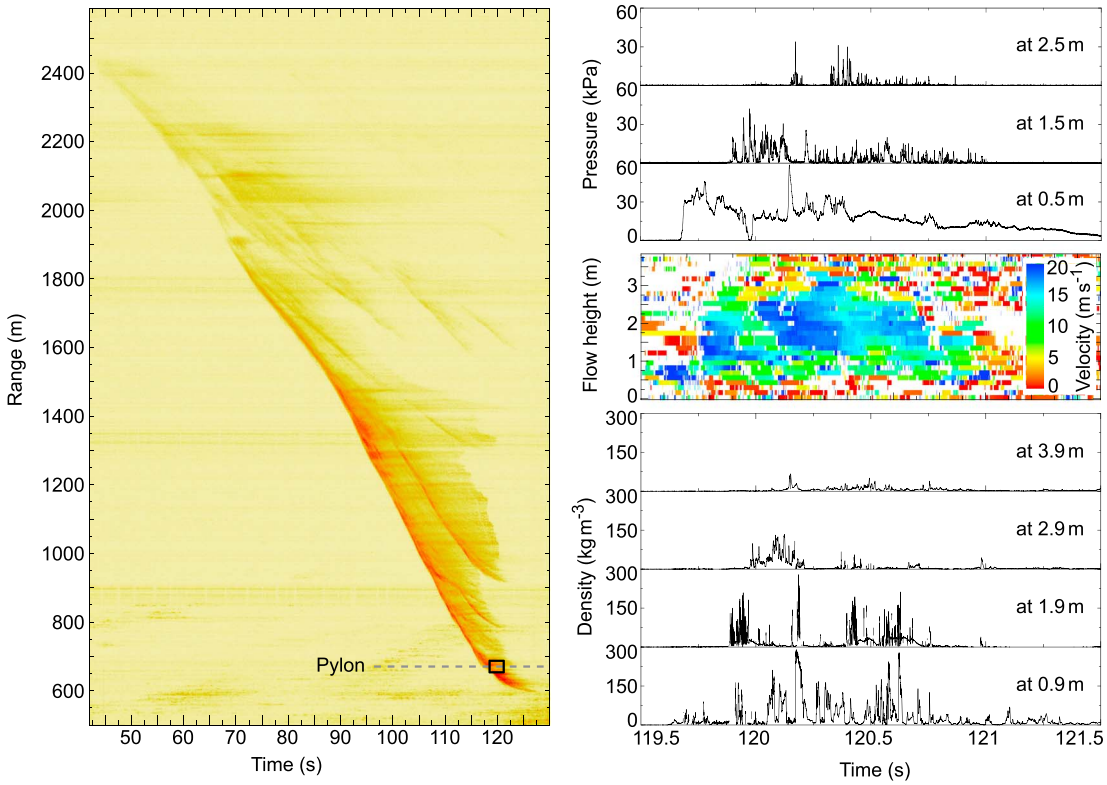

Figure 12. Avalanche #20150003. The left panel shows the GEODAR plot. The avalanche stops around 50 m below the pylon. The right panels, from top to bottom, show the avalanche pressure, velocity, and density measured at the pylon.

The velocity profile of a structure changes drastically during the deposition phase. Figure 14 shows a velocity profile corresponding to avalanche #20150003. The profile is arcuate with large shearing occurring at both boundaries and preferential deposition occurring at the lower boundary. A coherent movement of particles is only present in a small central flow region. This mesoscale structure finally starves over the next 50 m.

The mesoscale characteristic size varies among avalanches. For avalanche #20150016 the largest structures are approximately 3–5 m long, while for avalanche #20163017 the largest internal mesoscale structure is about 12–14 m long, one of the largest in our data set. Note that the structures are higher than 4 m in both cases, but it is not possible to assess the precise height, because measurements are not performed in the upper part of the flow.

4.2. Coherent Structures in the Avalanche Pressure, Air Pressure, and Density Data

Density measurements shown in the right panel of Figure 14 and in the bottom right panel of Figure 12 show that, even in a starving avalanche, average density in the intermittency region can easily be as high as 10–20 kg/m^3. The density signal in the intermittency region is characterized by large fluctuations, with high-density particle clusters typically reaching dense core densities of 200 kg/m^3 or more.

Figure 15 shows a comparison between the pressure exerted by a MSC structure (upper left panel) and the corresponding velocity for avalanche #20150016 (lower left panel). Peaks of pressure, corresponding to particle clusters, appear to accumulate into vertical or slightly curved bands. Interestingly, the scale of these bands is larger than single snow granules, but smaller than the MSC structure, suggesting that only a fraction of the overall MSC volume is occupied by high-density material.

A visualization of snow clustering is shown in the right panel of Figure 15, which displays the FMCW signal in cavern B of avalanche #20150016. Indeed, this figure shows intermittent bursts of dense snow clusters up to 9 m above the avalanche sliding surface. For avalanche #20160017, the impact of single snow granules has even been detected at 16 m above the ground, as previously shown in Figure 11. These data are remarkable in that it shows the presence of large granules very high in the flow for more than 2 s. This observation is relevant for understanding the forces that an avalanche could exert on a structure.

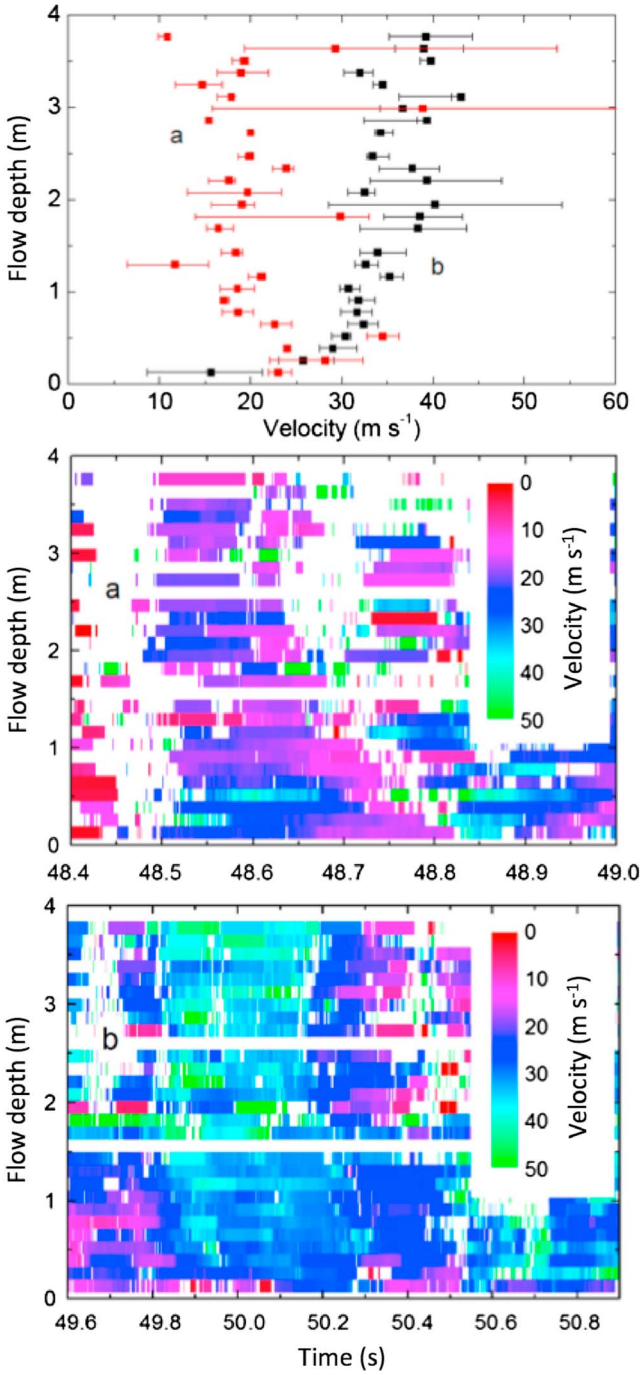

Figure 13. Velocities of two mesoscale structures in avalanche #20163017. Both structures are detached from the basal dense layer. The upper panel displays the velocity profiles of the frontal mesoscale structure (a) for the time window 48.52–48.68 s and of the fastest structure measured at the pylon (b) for the time window 49.84–50.17 s. Error bars are used as an indication of the velocity distribution inside each mesoscale structure and correspond to the 25%/75% quantiles. The middle and bottom panels display the entire velocity field for the frontal (middle panel) and fastest (bottom panel) structures.

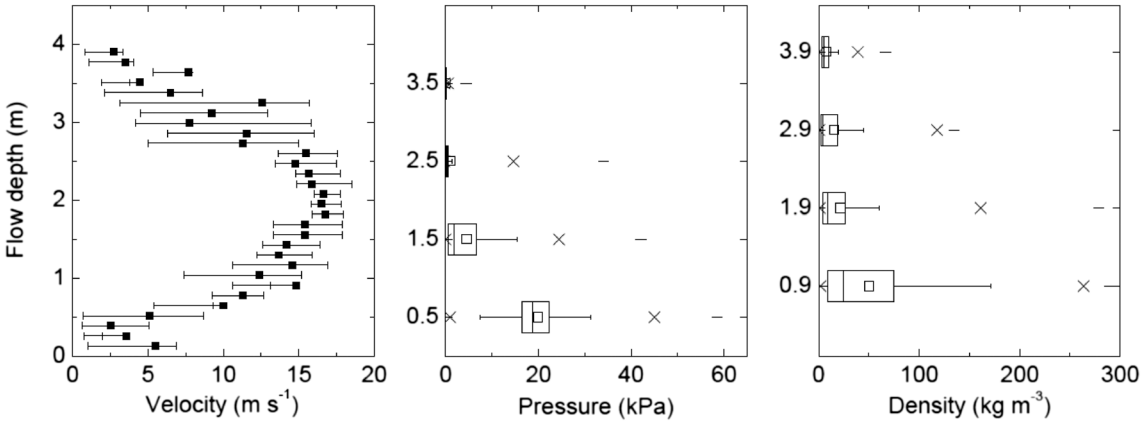

Figure 14. Velocity (left panel), pressure (middle panel), and density (right panel) profiles for a starving mesoscale structure in avalanche #20150003. In the left panel, error bars are used as an indication of the velocity distribution inside the mesoscale structure and correspond to the 25%/75% quantiles. In the middle and right panels, the box plots show the mean (square in box), median (line in box), 25%/75% quantiles (box), 5%/95% quantiles (whiskers), 1/99% quantiles (crosses), and minimum/maximum values (lines).

Finally, Figure 16 compares the mesoscale structures in the velocity distribution with air pressure and avalanche pressure data for avalanche #20163017. The air pressure data show a very strong harmonic signal, with a frequency of around 0.55 Hz, lasting more than 10 s (Figure 16 middle panel). The air pressure fluctuations are consistent with when the four major structures passed the lower part of the pylon (Figure 16 upper and lower panels), thus providing strong evidence that the mesoscale structures span the full flow depth of the avalanche.

4.3. Formation Mechanism for the Intermittency Region

Coherent structures, such as Horseshoe or Hairpin vortices, form in turbulent boundary layers at high Reynolds numbers (Kline et al., 1967). For PSAs the Reynolds number ranges from 10^6 to 10^9, resulting in a highly turbulent flow. On the upper surface of a PSA, there is high shear that gives rise to Kelvin-Helmholtz instabilities and turbulent entrainment of air, though this can be suppressed if the density difference is large enough. In addition, gravity currents have a large vortex at the head and, at higher Reynolds numbers, there may be several vortices in a chain behind the head (McElwaine & Turnbull, 2005; Turnbull & McElwaine, 2008). Figure 16 shows that the pressure increases as the PSA reached the pylon, then drops far below air pressure and then

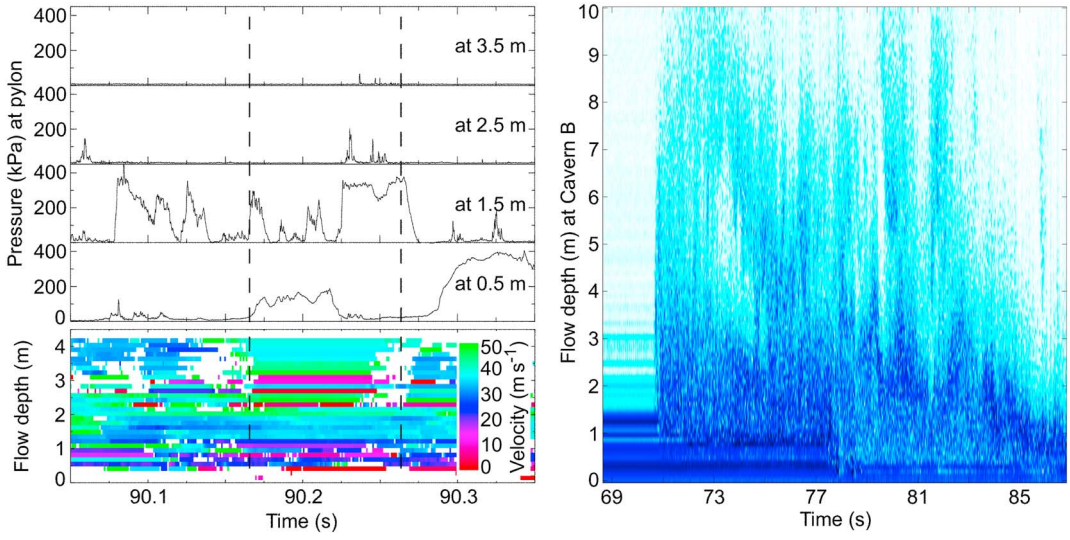

Figure 15. Avalanche #20150016. The upper left panel shows pressure measurements while the lower left panel shows the corresponding velocities. Dashed lines delineate the extent of the mesoscale structure. The right panel shows an frequency-modulated continuous-wave radar plot measured in cavern B corresponding to avalanche #20150016. The radar plot highlights the presence of intermittent bursts of dense snow clusters.

further oscillates between the passing of the mesoscale structures. Such a pressure signature may result from a train of vortices with the lowest pressure at the center, with the pressure gradient causing the centripetal acceleration necessary for circular motion. These vortices mean that there is large-scale recirculation within the avalanche frontal region, with vertical velocities that may exceed the front velocity.

Large quantities of material are disposable to be entrained by the coherent structures. At high enough Froude numbers the dense layer becomes highly agitated, possibly turbulent, and we expect the copious ejection of centimeter- to decimeter-scale granules under these conditions. Further material may also be ejected by the interaction between flow structures in the dense layer, such as surges (Köhler et al., 2016), or as a result of interactions with sharp changes in the terrain, or impact with obstacles, and we can not exclude that large pressure differences could induce a Darcy-like flow in the snow cover and directly lead to the fluidization of the static snow cover (Carroll et al., 2013; Louge et al., 2011).

We assume that the interaction between normal turbulence and grain size dynamics does produce new MSC structures which are thus different from the coherent structures known in classical turbulence. In homogeneous turbulence, vertical velocities around 10% of the mean velocity are expected. Such would be sufficient to entrain and suspend individual snow grains but not large granules. However, these coherent structures have long time scales and can have velocities of twice the front velocity, and thus they may directly entrain and lift much larger granules (Turnbull & McElwaine, 2008). In addition, the fine-particle air mixtures that characterize the mesoscale structures may have a density of up to 20 kg/m^3, which also dramatically increases the ability of the mixture to entrain and suspend large granules.

We now discuss quantitatively the size of granules that the air-snow mixture can entrain and suspend. We assume that the granules have a density of $\rho_p = 300-600$ kg/m^3 and a radius of $r = 10^{-3}-10^{-1}$ m (Issler et al., 1996; Schaer & Issler, 2001), which are typical values measured in cold avalanche deposits. We assume that the granules are roughly spherical and that the air-snow mixture has a density ρ_f, a viscosity η, and a vertical velocity v. The equation balancing fluid drag against gravity is then (Batchelor, 1967):

$$g\left(1-\frac{\rho_f}{\rho_p}\right)=\frac{3}{8r}C_d(\mathrm{Re})\frac{\rho_f}{\rho_p}v^2, \tag{4}$$

where g is the gravitational acceleration and Re is the particle Reynolds number:

$$\mathrm{Re}=\frac{2r\rho_f v}{\eta}. \tag{5}$$

We use the formula of Morsi and Alexander (1972) for C_d:

$$C_d(\mathrm{Re})=\frac{24}{\mathrm{Re}}+\frac{1}{1+\sqrt{\mathrm{Re}}}+0.422. \tag{6}$$

Many other similar formulae exist that interpolate between the exact low and high Reynolds number limits but they will make little difference to the results.

Equation (4) is solved numerically for the threshold v and the solutions are plotted in Figure 17. This threshold velocity v is the vertical velocity necessary to balance gravity. Close to the ground the velocity of a vortex is primarily horizontal, but this can accelerate granules, causing collisions and ejections that then move the granules into regions with higher vertical velocity. Figure 17 shows that pure air, with a density $\approx$1 kg/m^3, has too low a density to significantly affect the motion of large granules. A vertical velocity of 50 m/s would be necessary for a decimeter-sized granule, and for this to occur near the ground a much larger vortex velocity would be required. However, for a mixture of air and snow with a density of $\rho_f = 20$ kg/m^3 a velocity of only 10 m/s would be necessary to lift a decimeter-sized block.

Indeed, assuming that the vertical velocity of an MSC structure is of the same order as that of its translational velocity, vertical velocities can easily be larger than 20 m/s for the avalanches analyzed in this paper. Assuming that the average density of the MSCs is around $\approx$20 kg/m^3, as in the case of the smaller structure presented in this paper (Figure 12), we can conclude that all analyzed avalanches can easily entrain snow clusters with a size of at least 0.1 m.

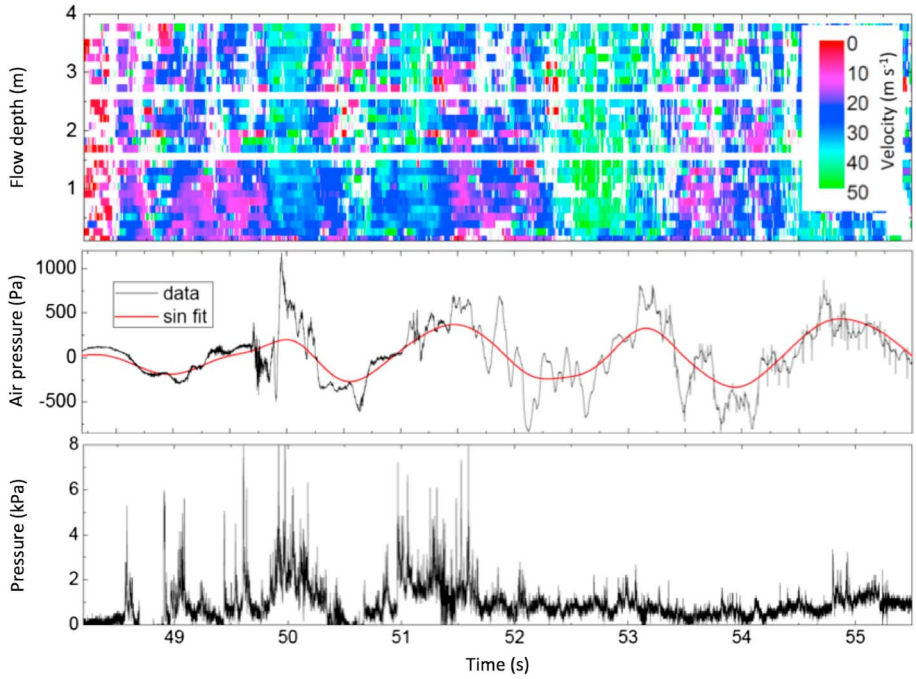

Figure 16. Avalanche #20163017. Mesoscale structures in the velocity data (upper panel) are compared with air pressure data collected with a Pitot sensor at 16 m above the ground (middle panel) and with pressure data measured at 5.5 m above the ground (lower panel). The red curve displays the low frequency harmonic in the air pressure signal, which is characterized by a mean period of 1.8 s and a frequency of 0.55 Hz (middle panel).

Thus, at the front of a PSA, where the air-snow mixture has its highest density and coherent vortices are most powerful, large quantities of decimeter-sized blocks can easily be lifted high in the avalanche. This is in agreement with FMCW radar measurements, which suggest that snow entrainment occurs largely at the avalanche front (Sovilla et al., 2006).

Even if we have no precise information on the lifespan of such structures, an indication can come from recent measurements performed with GEODAR data at VdlS. Köhler et al. (2016) showed that the frontal zone of powder avalanches is characterized by minor surges, interpreted to be clusters of denser material or rolling wave-like instabilities, which move faster than the leading edge and thus frequently overtake it. GEODAR plots shows that the lifespan of these structures is around 2–4 s and that they continuously regenerate.

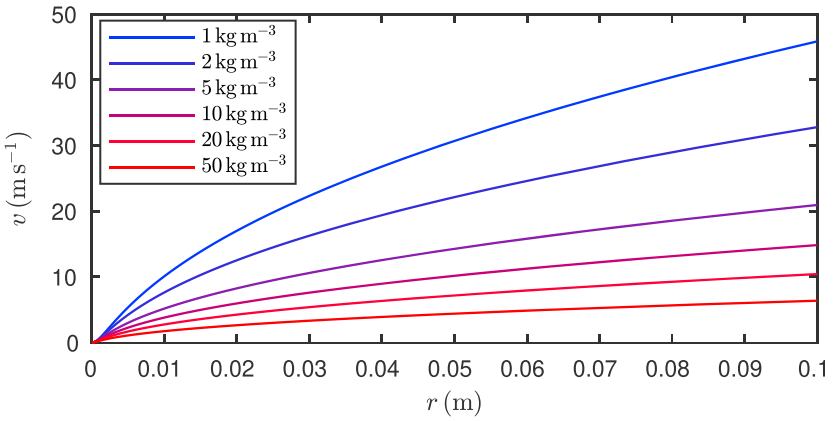

Figure 17. Threshold velocity v as a function of granule size r for different air-snow mixture densities ρ_f.

These features correspond to the mesoscale structures analyzed in this paper. Thus, our hypothesis is that the intermittency region is the result of the creation and regeneration of instabilities and vortices that transport material aloft for a few seconds and then decay.

These structures have an important effect on avalanche dynamics. As shown by Köhler et al. (2016), the frontal region of PSAs is controlled by the generation and evolution of such structures. In particular, these structures can move ahead of the dense basal layer and reach farther, explaining the presence of a three-layered structure in the deposit of PSAs (Issler et al., 1996). Further, these structures provide a justification for the finding of large particles far away from the deposit or flow region of the dense basal layer (Issler et al., 1996; Schaer & Issler, 2001).

We expect that the processes investigated in this paper may be relevant not only for PSAs but also for other complex geophysical flows, such as turbidity currents (Meiburg et al., 2012) and pyroclastic density currents. Indeed, a recent laboratory study on the coupling of turbulent and nonturbulent flow regimes within pyroclastic density currents also shows the existence of a region of intermediate particle concentrations. In this region there is a strong interaction between the air and the particles and the formation of mesoscale clusters which they argue controls the mass balance between the suspension and dense basal layer (Breard et al., 2016).

This paper strongly suggests that the intermittency region is critical to the dynamics of avalanches. The development of a model that includes the intermittency region should therefore be considered the most important next step in the development of PSA models (Bartelt et al., 2016; Issler & Gauer, 2008). The data from this paper suggest that both particle-particle and particle-fluid interactions are important, as well as the presence of coherent structures. Future work should also consider whether there is any connection to the *light flow* regime observed in open channel flows at Froude numbers greater than 3.5, where the surface becomes unstable and is so highly agitated that there is air entrainment and the development of a middle zone (Schaerer & Salway, 1980, and references therein).

5. Conclusions

The data from VdIS clearly show that the frontal zone of powder avalanches is characterized by the presence of MSC structures that are responsible for driving large snow granules and snow clusters high into the air. Indeed, we have shown direct evidence of intermittent bursts of decimeter-sized, high-density snow granules reaching large heights at the front of PSAs. We call this the intermittency region (Köhler et al., 2018). This flow regime increases in length and significance with avalanche size, which may in extreme cases extend for almost the entire flow.

We interpret the coherent structures near the frontal zone to be large vortices that always develop in gravity currents with high Reynolds numbers and that are closely associated with the lobe-and-cleft structure. Further back in the avalanche, the structures are most likely more generic, with smaller horseshoe and hairpin vortices forming at the base of the suspension cloud and then detaching.

The intricate interaction between coherent structures caused by normal turbulence and grain size dynamics with a large size distribution gives rise to the MSC structures. We may expect that those coherent mesoscale structures starve when large granules are no longer available. In contrast, they can grow in size, and their lifespan increases, when larger granules are increasingly available.

Further, by showing evidence that MSC structures stem from a complicated interaction between turbulent coherent structures and grain size dynamics involving a wide range of particles from fine snow/ice grains (less than 0.5 mm) to large granules (several centimeters or more), we claim that the concept of a pure PSA (suspension) is a theoretical concept that probably does not exist in nature. The current study could help in designing new laboratory experiments with tests in a water tank involving gravity currents but mixed with some larger sized particles.

The interaction between coherent structures and particles is extremely complicated, particularly in the highly non-Boussinesq case, because large density gradients exert a strong damping effect on vertical fluid motion. However, a model for this process is essential if mass and momentum transport are to be modeled accurately.

If one desires to reproduce the intermittency in numerical simulations, turbulence has to be modeled directly or, at the very least, through Large-Eddy Simulation. However, the effects of intermittency that are relevant

for practical applications can be accounted for in a much simpler way, as it is shown in numerous models of turbulent closure. In this last case, pressure fluctuations can be extracted from the models, thus allowing a comparison of the statistical properties of model predictions with experimental data.

Finally, these measurements suggest that intermittency and MSC structures also play an important role in other geophysical flows, such as pyroclastic and turbidity currents.

Acknowledgments
The authors would like to thank the avalanche dynamics team and logistics staff of the WSL/SLF for their support in the experiments. We are grateful to Michel Louge for designing of the density sensors and for invaluable discussions on powder avalanche dynamics and to Melissa Dawes for the language editing. The research was partially funded by the Swiss National Science Foundation (SNSF) project *High Resolution Radar Imaging of Snow Avalanches*, grant 200021_143435, and founding for the test site and infrastructure was provided by the SNSF R'EQUIP project *Snow Avalanches in the Swiss experiment*, grant 206021_113069/1 and by the canton of Valais. We gratefully thank Dieter Issler and two anonymous reviewers whose suggestions helped improve and clarify this manuscript. The data presented in this paper are available in the open access data repository Zenodo, which is financed by the Horizon 2020 project OpenAIRE and hosted by CERN. The associated entry can be accessed via B. Sovilla, J. N. McElwaine, and A. Köhler (2018), The intermittency regions of powder snow avalanches [Data set]. Zenodo. https://doi.org/10.5281/zenodo.1415456.

References

Ammann, W. J. (1999). A new Swiss test site for avalanche experiments in the Vallée de la Sionne/Valais. *Cold Regions Science and Technology*, *30*, 3–11. https://doi.org/10.1016/S0165-232X(99)00010-5

Ancey, C. (2004). Powder snow avalanches: Approximation as non-Boussinesq clouds with a Richardson number-dependent entrainment function. *Journal of Geophysical Research*, *109*, F01005. https://doi.org/10.1029/2003JF000052

Ash, M., Brennan, P. V., Keylock, C. J., Vriend, N. M., McElwaine, J. N., & Sovilla, B. (2014). Two-dimensional radar imaging of flowing avalanches. *Cold Regions Science and Technology*, *102*, 41–51. https://doi.org/10.1016/j.coldregions.2014.02.004

Bartelt, P., Buser, O., Valero, C. V., & Buehler, Y. (2016). Configurational energy and the formation of mixed flowing/powder snow and ice avalanches. *Annals of Glaciology*, *57*(71), 179–188. https://doi.org/10.3189/2016AoG71A464

Batchelor, G. (1967). *An introduction to fluid dynamics*. Cambridge, England: Cambridge University Press.

Bonnecaze, R. T., Huppert, H. E., & Lister, J. R. (1996). Patterns of sedimentation from polydisperse turbidity currents. *Proceedings of the Royal Society A*, *452*, 2247–2261. https://doi.org/10.1098/rspa.1996.0120

Bozhinskiy, A. N., & Losev, K. S. (1998). The fundamentals of avalanche science (Report No. 55). Davos Dorf, Switzerland: Eidg.Institut f.Schnee- und Lawinenforschung.

Breard, E. C. P., Lube, G., Jones, J. R., Dufek, J., Cronin, S. J., Valentine, G. A., & Moebis, A. (2016). Coupling of turbulent and non-turbulent flow regimes within pyroclastic density currents. *Nature Geoscience*, *9*(10), 767–771. https://doi.org/10.1038/ngeo2794

Carroll, C. S., Louge, M. Y., & Turnbull, B. (2013). Frontal dynamics of powder snow avalanches. *Journal of Geophysical Research: Earth Surface*, *118*, 913–924. https://doi.org/10.1002/jgrf.20068

Dent, J. D., Burrell, K. J., Schmidt, D. S., Louge, M. Y., Adams, E., & Jazbutis, T. G. (1998). Density, velocity and friction measurements in a dry-snow avalanche. *Annals of Glaciology*, *26*, 247–252. https://doi.org/10.3189/1998AoG26-1-247-252

Faug, T., Turnbull, B., & Gauer, P. (2018). Looking beyond the powder/dense flow avalanche dichotomy. *Journal of Geophysical Research: Earth Surface*, *123*, 1183–1186. https://doi.org/10.1002/2018JF004665

Grigoryan, S., Urubayev, N., & Nekrasov, I. (1982). Experimental investigation of an avalanche air blast (in Russian). *Data Glaciology Student*, *44*, 87–93.

Gubler, H., & Hiller, M. (1984). The use of microwave FMCW radar in snow and avalanche research. *Cold Regions Science and Technology*, *9*, 109–119. https://doi.org/10.1016/0165-232X(84)90003-X

Issler, D. (1999). European avalanche test sites. Overview and analysis in view of coordinated experiments (Report No. 59). Davos Dorf, Switzerland: Eidg.Institut f.Schnee- und Lawinenforschung.

Issler, D., Errera, A., Priamo, S., Gubler, H., Teufen, B., & Krummenacher, B. (2008). Inferences on flow mechanisms from snow avalanche deposits. *Annals of Glaciology*, *49*, 187–192. https://doi.org/10.3189/172756408787814915

Issler, D., & Gauer, P. (2008). Exploring the significance of the fluidized flow regime for avalanche hazard mapping. *Annals of Glaciology*, *49*, 193–198. https://doi.org/10.3189/172756408787814997

Issler, D., Gauer, P., Schaer, M., & Keller, S. (1996). Staublawinenereignisse im Winter 1995: Seewis (GR), Adelboden (BE) und Col du Pillon (VD) (Mittlg.No. 694). Davos Dorf, Switzerland: Eidg.Institut f.Schnee- und Lawinenforschung.

Issler, D., Jenkins, J. T., & McElwaine, J. N. (2018). Comments on avalanche flow models based on the concept of random kinetic energy. *Journal of Glaciology*, *64*(243), 148–164. https://doi.org/10.1017/jog.2017.62

Jamieson, B. (Ed.) (2000). *Backcountry avalanche awareness*. Canada: Canadian Avalanche Association.

Köhler, A., McElwaine, J. N., & Sovilla, B. (2018). GEODAR Data and the flow regimes of snow avalanches. *Journal of Geophysical Research: Earth Surface*, *123*, 1272–1294. https://doi.org/10.1002/2017JF004375

Köhler, A., McElwaine, J. N., Sovilla, B., Ash, M., & Brennan, P. V. (2016). The dynamics of surges in the 3 February 2015 avalanches in Vallée de la Sionne. *Journal of Geophysical Research: Earth Surface*, *121*, 2192–2210. https://doi.org/10.1002/2016JF003887

Kern, M. A., Bartelt, P., Sovilla, B., & Buser, O. (2009). Measured shear rates in large dry and wet snow avalanches. *Journal of Glaciology*, *55*(190), 327–338. https://doi.org/10.3189/002214309788608714

Kline, S., Reynolds, W., Schraub, F., & Runstadler, P. (1967). The structure of turbulent boundary layers. *Journal of Fluid Mechanics*, *30*(4), 741–773. https://doi.org/10.1017/S0022112067001740

Konopliv, N. A., Llewellyn-Smith, S. G., McElwaine, J. N., & Meiburg, E. (2016). Modeling gravity currents without an energy closure. *Journal of Fluid Mechanics*, *789*, 806–829. https://doi.org/10.1017/jfm.2015.755

Lehning, M., Bartelt, P., Brown, B., Fierz, C., & Satyawali, P. (2002). A physical SNOWPACK model for the Swiss avalanche warning. PART II: Snow microstructure. *Cold Regions Science and Technology*, *35*, 147–167. https://doi.org/10.1016/S0165-232X(02)00073-3

Louge, M. Y., Carroll, C. S., & Turnbull, B. (2011). Role of pore pressure gradients in sustaining frontal particle entrainment in eruption currents: The case of powder snow avalanches. *Journal of Geophysical Research*, *116*, F04030. https://doi.org/10.1029/2011JF002065

Louge, M. Y., Steiner, R., Keast, S., Decker, R., Dent, J., & Schneebeli, M. (1997). Application of capacitance instrumentation to the measurement of density and velocity of flowing snow. *Cold Regions Science and Technology*, *25*(1), 47–63. https://doi.org/10.1016/S0165-232X(96)00016-X

McElwaine, J. N., & Turnbull, B. (2005). Air pressure data from the Vallée de la Sionne avalanches of 2004. *Journal of Geophysical Research*, *110*, F03010. https://doi.org/10.1029/2004JF000237

Meiburg, E., McElwaine, J. N., & Kneller, B. (2012). Turbidity currents and powder snow avalanches. In H. Fernando (Ed.), *Handbook of environmental fluid dynamics* (Vol. 1, chap. 42, pp. 557–573). England: Taylor & Francis. https://doi.org/10.1201/b14241-46

Morsi, A., & Alexander, S. (1972). An investigation of particle trajectories in two-phase flow system. *Journal of Fluid Mechanics*, *55*, 193–208. https://doi.org/10.1017/S0022112072001806

Nishimura, K., Maeno, N., Kawada, K., & Izumi, K. (1993). Structures of snow cloud in dry-snow avalanches. *Annals of Glaciology*, *18*, 173–178. https://doi.org/10.3189/S0260305500011459

Norem, H. (1991). Estimating snow avalanche impact pressure on towers. In *Proceedings of a Workshop on Avalanche Dynamics* (pp. 14–19). Switzerland.

Rastello, M., Rastello, F., Bellot, H., Ousset, F., Dufour, F., & Meier, L. (2011). Size of snow particles in a powder-snow avalanche. *Journal of Glaciology*, *57*(201), 151–156. https://doi.org/10.3189/172756401781819283

Sanford, L. P. (1997). Turbulent mixing in experimental ecosystem studies. *Marine Ecology Progress Series*, *161*, 265–293. https://doi.org/10.3354/meps161265

Schaer, M., & Issler, D. (2001). Particle densities, velocities and size distribution in large avalanches from impact-sensor measurements. *Annals of Glaciology*, *32*, 321–327. https://doi.org/10.3189/172756401781819409

Schaerer, P., & Salway, A. A. (1980). Seismic and impact-pressure monitoring of flowing avalanches. *Journal of Glaciology*, *26*(94), 179–187. https://doi.org/10.3189/S0022143000010716

Shimizu, H., Huzioka, T., Akitaya, E., Narita, H., Nakagawa, M., & Kawada, K. (1980). A study on high-speed avalanches in the Kurobe canyon, Japan. *Journal of Glaciology*, *26*(94), 141–151. https://doi.org/10.3189/S0022143000010686

Simpson, J. E. (1997). *Gravity currents: In the environment and the laboratory*. England: Cambridge University Press.

Sovilla, B., Burlando, P., & Bartelt, P. (2006). Field experiments and numerical modeling of mass entrainment in snow avalanches. *Journal of Geophysical Research*, *111*, F03007. https://doi.org/10.1029/2005JF000391

Sovilla, B., McElwaine, J. N., & Louge, M. Y. (2015). The structure of powder snow avalanches. *Comptes Rendus Physique*, *16*(1), 97–104. https://doi.org/10.1016/j.crhy.2014.11.005

Sovilla, B., McElwaine, J. N., Schaer, M., & Vallet, J. (2010). Variation of deposition depth with slope angle in snow avalanches: Measurements from Vallée de la Sionne. *Journal of Geophysical Research*, *115*, F02016. https://doi.org/10.1029/2009JF001390

Sovilla, B., Schaer, M., Kern, M., & Bartelt, P. (2008). Impact pressures and flow regimes in dense snow avalanches observed at the Vallée de la Sionne test site. *Journal of Geophysical Research*, *113*, F01010. https://doi.org/10.1029/2006JF000688

Sovilla, B., Schaer, M., & Rammer, L. (2008). Measurements and analysis of full-scale avalanche impact pressure at the Vallée de la Sionne test site. *Cold Regions Science and Technology*, *51*, 122–137. https://doi.org/10.1016/j.coldregions.2007.05.006

Steinkogler, W., Gaume, J., Löwe, H., Sovilla, B., & Lehning, M. (2015). Granulation of snow: From tumbler experiments to discrete element simulations. *Journal of Geophysical Research: Earth Surface*, *120*, 1107–1126. https://doi.org/10.1002/2014JF003294

Steinkogler, W., Sovilla, B., & Lehning, M. (2014). Influence of snow-cover properties on avalanche dynamics. *Cold Regions Science and Technology*, *97*, 121–131. https://doi.org/10.1016/j.coldregions.2013.10.002

Sukhanov, G. (1982). The mechanism of avalanche air blast formation as derived from field measurements (in Russian). *Data Glaciology Student*, *44*(94–98).

Turnbull, B., & McElwaine, J. N. (2008). Experiments on the non-Boussinesq flow of self-igniting suspension currents on a steep open slope. *Journal of Geophysical Research*, *113*, F01003. https://doi.org/10.1029/2007JF000753

Vriend, N. M., McElwaine, J. N., Sovilla, B., Keylock, C. J., Ash, M., & Brennan, P. V. (2013). High-resolution radar measurements of snow avalanches. *Geophysical Research Letters*, *40*, 727–731. https://doi.org/10.1002/grl.50134

Zwinger, T., Kluwick, A., & Sampl, P. (2003). Numerical simulation of dry-snow avalanche flow over natural terrain. In K. Hutter, & N. Kirchner (Eds.), *Dynamic response of granular and porous materials under large and catastrophic deformations, Lecture Notes in Applied and Computational Mechanics* (Vol. 11, pp. 161–194). Berlin, Germany: Springer.